Density and atomic coordination dictate vibrational characteristics and thermal conductivity of amorphous silicon carbide

Sandip Thakur,[1] Connor Jaymes Dionne,[1] Pravin Karna,[1] Sean W. King,[2] William Lanford,[3] Han Li,[2] Shouvik Banerjee,[2] Devin Merrill,[2] Patrick E. Hopkins,[4,5,6] and Ashutosh Giri[1,*]

[1]*Department of Mechanical, Industrial, and Systems Engineering, University of Rhode Island, Kingston, Rhode Island 02881, USA*
[2]*Intel Corporation, Logic Technology Development, Hillsboro, Oregon 97124, USA*
[3]*Physics Department, University at Albany, Albany, New York 12206, USA*
[4]*Department of Mechanical and Aerospace Engineering, University of Virginia, Charlottesville, Virginia 22904, USA*
[5]*Department of Materials Science and Engineering, University of Virginia, Charlottesville, Virginia 22904, USA*
[6]*Department of Physics, University of Virginia, Charlottesville, Virginia 22904, USA*

(Received 29 June 2022; revised 31 July 2022; accepted 22 August 2022; published 2 September 2022)

Silicon carbide coatings and thin films are used for a wide array of applications ranging from thermal barrier coatings to microelectronics. In this paper, we report on the role of mass density and atomic coordination on the fundamental vibrational characteristics and thermal conductivity of amorphous silicon carbide systems through a combination of experiments and systematic atomistic simulations. We use time domain thermoreflectance to show that the thermal conductivity of hydrogenated amorphous silicon carbide can be increased twofold with ∼40% increase in the mass density. A simple description of thermal transport applicable to a range of amorphous solids where diffusion of thermal energy is predominantly driven by nonpropagating modes cannot fully describe our experimental measurements. Our molecular dynamics simulations in conjunction with our lattice dynamics calculations shed light on the intrinsic role of atomic coordination in dictating the contributions from both propagating and nonpropagating modes in amorphous silicon carbide structures. More specifically, we find that as the concentration of sp^3 hybridized carbon atoms is increased by up to 10% with increasing mass densities, the contribution from propagons can be increased from ∼25% to ∼40%, after which further increments in the mass density and the sp^3 fraction does not lead to higher contributions from propagons. In contrast, contributions from the nonpropagating modes increases monotonically with increasing mass density and sp^3 hybridization. Our results pave a path forward to manipulate the thermal conductivity of amoprhous silicon carbide systems based on varying the atomic coordination.

DOI: 10.1103/PhysRevMaterials.6.094601

I. INTRODUCTION

Amorphous silicon carbide is a wide band-gap semiconductor used in a variety of technologically relevant applications such as in microelectronics [1], photovoltaics [2], light emitting diodes [3], membranes for microfluidic devices [4], and thermal barrier coatings, to name a few [5]. Depending on the fabrication procedure and conditions, the microstructure and average coordination number $\langle r \rangle$ of these amorphous materials can be varied across a wide range [6], which can in turn impact their physical properties and dictate their functionalities in the aforementioned applications. For example, reducing $\langle r \rangle$ lowers the dielectric constant for hydrogenated amorphous silicon carbide (a-SiC:H) films used for very large-scale integrated interconnects as dielectric insulators [1]. However, the decrease in $\langle r \rangle$ has also been shown to monotonically reduce the Young's modulus, thus compromising the mechanical integrity of the insulating layers [7]. Recently, we have shown that the thermal conductivity of amorphous carbon and hydrogenated amorphous silicon nitride (a-SiN_x:H) can be decreased by reducing $\langle r \rangle$ [8,9], demonstrating an efficient route to manipulate the thermal transport properties of amorphous materials through varying their microstructural coordination. However, an in-depth understanding of the role of microstructures on the vibrational properties and thermal conductivity of amorphous silicon carbide-based systems has remained elusive, which is the goal of the current paper.

In general, manipulating the thermal conductivity of amorphous solids below the so-called minimum limit where energy transport is carried by the random walk of vibrations is conventionally thought to be a difficult task [10]. This is mainly because of the fact that lowering thermal conductivity below the minimum limit requires restricting the mean-free paths of vibrations to be on the order of the atomic spacings. However, recent findings on amorphous silicon have shown that a significant proportion of heat can be carried by phononlike vibrations [11–14], which opens an avenue to tune the thermal properties of amorphous solids through scattering of long wavelength propagating modes. Over the years, this approach has been applied to achieve ultralow thermal conductivities in crystalline and quasicrystalline fully dense solids through introduction of nanostructured interfaces [15–21] or

*ashgiri@uri.edu

by varying the local bonding environment [17,22–25], which can scatter the heat-carrying phonons. Unlike in crystalline solids, however, the heat-carrying vibrations in amorphous materials are categorized as propagons that are propagating, phononlike vibrations and diffusons that are nonpropagating but delocalized modes [26,27]. The high-frequency localized modes—locons—also constitute the vibrational spectrum in amorphous solids but these modes do not contribute to heat conduction directly due to their localized nature. Therefore, fully understanding and efficiently manipulating the categorical vibrations in amorphous solids via control of the microstructure to ultimately impact the overall heat conduction can be beneficial for a range of applications such as in thermoelectrics, thermal barrier coatings, or in amorphous dielectric layers in microelectronic devices where thermal transport can be the limiting factor dictating the functionality of the devices [28–30].

In this paper, we study the thermal properties of amorphous silicon carbide systems through a combination of experiments and simulations to reveal their structure-property relationship. More specifically, through chemical, mechanical, vibrational, and structural analysis in conjunction with time domain thermoreflectance (TDTR) measurements, we show that the coordination number and mass density can influence the measured thermal conductivities by a factor of 2 in thin films of a-SiC:H. We find that the thermal conductivity increases monotonically from $\sim 0.9\,\mathrm{W\,m^{-1}\,K^{-1}}$ to $\sim 1.9\,\mathrm{W\,m^{-1}\,K^{-1}}$ with mass densities increasing from $\sim 2\,\mathrm{g\,cm^{-3}}$ to $\sim 2.9\,\mathrm{g\,cm^{-3}}$. Fourier-transform infrared spectroscopy (FTIR) measurements on the a-SiC:H samples reveal that increasing mass density leads to a higher fraction of Si-C bonds, which increases the average atomic coordination of the films. Complementary molecular dynamics (MD) simulations and lattice dynamics (LD) calculations on a-SiC show that the mass density has major implications on the structural and vibrational properties of these materials. In particular, we find that the increase in density leads to an increase in the sp^3 concentration. Furthermore, we find that the range of vibrational modes that are described as propagons increases to higher frequencies as density (and sp^3 content) is increased. Evidently, the contribution from propagons can be increased from $\sim$25% to $\sim$40% by increasing the fraction of carbon with sp^3 hybridization to $\geqslant$ 10% (or above densities of $\sim 2.2\,\mathrm{g\,cm^{-3}}$) in a-SiC. In contrast, the diffuson-driven thermal conductivity increases monotonically for the entire mass density range (from 1.5 to $3.2\,\mathrm{g\,cm^{-3}}$) studied in this paper.

II. EXPERIMENTAL DETAILS AND RESULTS

A. Sample preparation and characterizations

The a-SiC:H films investigated in this paper are deposited on 300-mm-diameter Si (001) wafers by plasma-enhanced chemical vapor deposition methods that have been described in detail previously [6]. Briefly, process variables such as pressure, organosilane flow rate, and applied radio frequency power are modulated to produce a-SiC:H films with varying hydrogen content and mass density. To further modulate hydrogen content and mass density, some a-SiC:H films are given a postdeposition anneal at temperatures of $500 - 700\,^{\circ}\mathrm{C}$ for 1 hour as described previously [31].

After deposition and annealing, all samples are subjected to a variety of thin film characterization including Fourier transform infrared spectroscopy (FTIR) [32], nanoindentation [6], and combined Rutherford backscattering spectroscopy and nuclear reaction analysis (RBS-NRA) [33] the details of which can be found in the provided citations. Briefly, FTIR is utilized to look at the chemical bond structure of the a-SiC:H films and employed a Nicolet Magna-IR 860 spectrometer. Transmission FTIR spectra are collected with $4\,\mathrm{cm^{-1}}$ resolution and a pre-scan of a bare Si wafer is used for background subtraction [32]. Nanoindentation is utilized to characterize the elastic modulus and hardness of the a-SiC:H films. Load-displacement is measured using a NanoXP nanoindenter with a Berkovich diamond tip. A Poisson's ratio is assumed for all a-SiC:H films [6]. RBS-NRA measurements are performed at the U. Albany Dynamitron Laboratory to determine the full atomic composition and mass density of the a-SiC:H films. The hydrogen concentration is determined using the ^{15}N nuclear reaction method, C concentration is determined using deuteron nuclear reactions, and Si content is determined by classic $2\,\mathrm{MeV}$ ^{4}He RBS [33]. The mass density of the a-SiC:H films are confirmed by additional x-ray reflectivity measurements and found to agree with RBS-NRA to within $\pm(0.1\,\mathrm{g\,cm^{-3}})$ [6]. Film thicknesses are obtained via a spectroscopic ellipsometry-based technique [6].

B. Thermal property measurements

The thermal conductivity of six different samples (see Table I) are measured using TDTR, for which the details of the experimental setup and the analysis procedure can be found in Refs. [34–36]. Briefly, our TDTR setup utilizes a Mai Tai Spectra Physics laser that emanates 100 fs pulses at 12.5 ns time intervals (80 MHz repetition rate). The laser beam is separated into pump and probe paths where the pump pulses are modulated at prescribed frequencies of either 2 MHz or 10 MHz, which creates a periodic heating event at the sample surface. Prior to the TDTR measurements, a thin aluminum transducer layer of $\sim$80 nm thickness is deposited on top of the samples. We measure the ratio of in-phase (V_{in}) to out-of-phase (V_{out}) voltage of the probe beam with a lock-in amplifier as a function of delay time and fit the data with a thermal model that accounts for the three layers (i.e., Al/a-SiC:H/Si substrate). The thickness of the Al transducer used as an input parameter in the thermal model is measured via picosecond acoustics [37,38]. The $1/e^2$ pump and probe radii are 11 μm and 7 μm, respectively. The multiple modulation frequencies are used to fit the thermal conductivity and volumetric heat capacity simultaneously, as we discuss in more detail below.

Figure 1(a) shows the representative TDTR data along with our best fits from the thermal model for three a-SiC:H thin film samples at varying mass densities (see Table I). We iterate the values of the thermal boundary conductance between the Al transducer and the thin film (h_{k}) and the thin film thermal conductivity ($\kappa_{\mathrm{a\text{-}SiC:H}}$) to achieve the best fits. The values of the other input parameters (such as the heat capacity and thermal conductivity) of the aluminum transducer and silicon substrate are taken from literature [39]. To determine

TABLE I. Values for the measured thicknesses (d, as determined via elipsometry), mass densities (ρ), compositions (as determined via RBS), thermal conductivities (κ, as determined via TDTR) and Young's modulus (E, as determined via nanoindentation).

a-SiC:H	Thickness, d (nm)	% C (±5%)	% Si (±5%)	% H (±5%)	Density, ρ (g cm^{-3}) (±0.1)	κ (W m^{-1}K^{-1})	E (GPa)
Sample 1	500	33.18	29.39	37.44	2.1	1.02 ± 0.1	127 ± 4
Sample 2	600	35.60	31.21	33.19	2.1	1.06 ± 0.11	139 ± 5
Sample 3	600	42.75	37.89	19.36	2.1	0.96 ± 0.09	
Sample 4	600	37.39	37.21	25.39	2.5	1.47 ± 0.2	210 ± 6
Sample 5	600	38.34	37.69	23.97	2.5	1.44 ± 0.18	214 ± 6
Sample 6	500	38.00	37.74	24.25	2.9	1.92 ± 0.26	240 ± 7

the heat capacities of our films, we use a 100 nm a-SiC:H film at 2.5 g cm^{-3} for which our thermal model is sensitive to both heat capacity and thermal conductivity of the film at the low modulation frequency. This is exemplified in Fig. 1(b), showing the contour plot of the residual error at our low- and high-modulation frequencies. We determine the heat capacity of a-SiC:H at 2.5 g cm^{-3} to be 1.9 ± 0.3 J cm^{-3} K^{-1} from

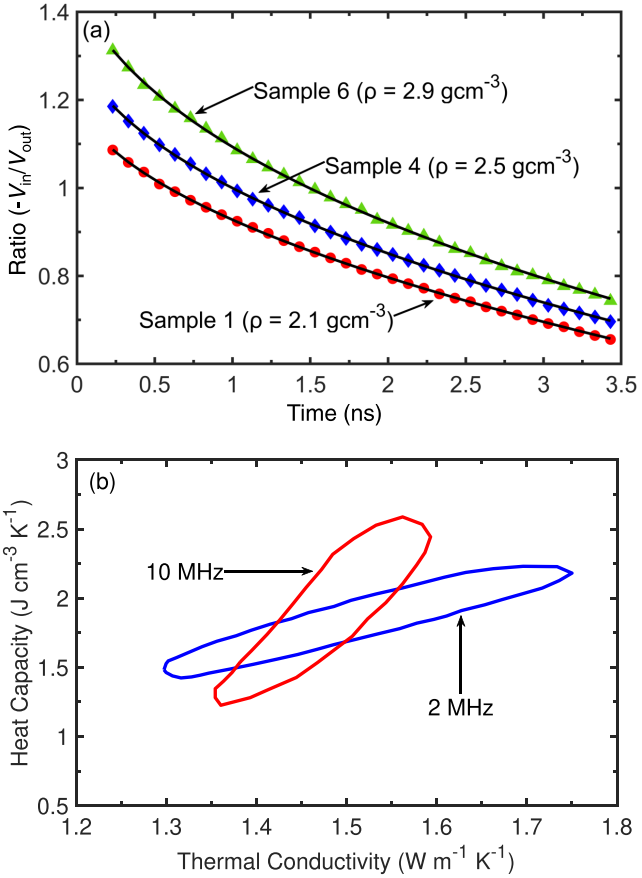

FIG. 1. (a) Representative TDTR data for Al/a-SiC:H/Si-substrate samples and their corresponding best-fit thermal models. We fit the thermal model to the ratio of the in-phase (V_{in}) and out-of-phase (V_{out}) voltage signals as a function of pump-probe delay time. (b) Sensitivity residual plot showing the interrelationship between thermal conductivity and heat capacity of a 100-nm-thick a-SiC:H sample at 2 MHz and 10 MHz pump modulation frequencies. The value of heat capacity chosen for our thermal model is taken from the intersection between the two contours.

the overlapping region between the two frequencies. For the thicker samples with varying densities (where TDTR is unable to independently measure both the heat capacity and thermal conductivity), we scale the heat capacity with respect to the densities of the films, which we use in the thermal model to predict the thermal conductivities as given in Table I; the sensitivity of the heat capacity and thermal conductivity for the thicker (∼600 nm) samples in our thermal model are similar and, as such, we are unable to determine the two parameters separately from our measurements. The uncertainties for our thermal conductivity measurements include the error from our heat-capacity determination, aluminum film thickness, and variability in the measured ratio at different spots on the samples of interest.

Figure 2 shows the thermal conductivity as a function of mass density of our a-SiC:H thin films. We also include the result of a 2.5 g cm^{-3} mass density film measured with TDTR at the University of Virginia, which matches well with results from our measurements carried out at the University of Rhode

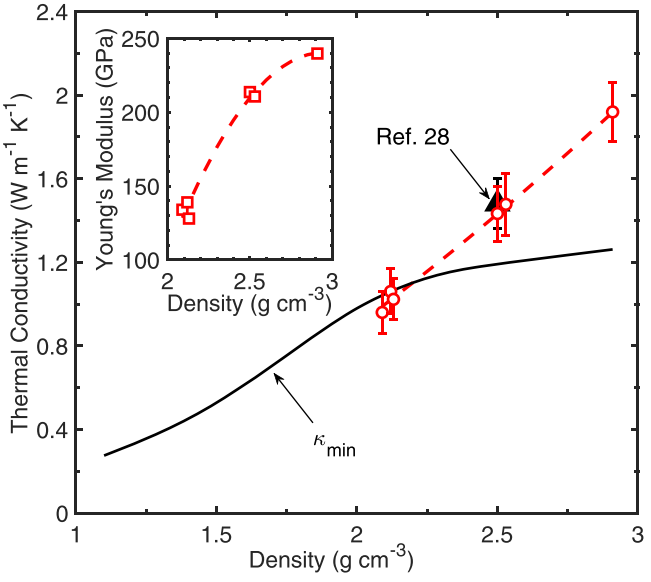

FIG. 2. TDTR measured thermal conductivities of a-SiC:H films as a function of mass density (circles represent measurements taken at University of Rhode Island, whereas the solid triangle represent data taken at the University of Virginia). The predictions from the minimum thermal conductivity model (solid line) for a-SiC:H is also included for comparison. Inset: Measured Young's modulus (E) as a function of mass density for our a-SiC:H films.

Island. Overall, we find that as the density of our films are increased by 40%, the thermal conductivity increases by almost a factor of 2.

We compare our results to the minimum thermal conductivity model that is usually applied to pure amorphous solids, where it is assumed that the lifetime of the vibrational modes is limited to one-half the period of oscillation (and where energy is transferred predominantly through nonpropagating modes) given as [40]

$$\kappa_{\min} = \left(\frac{\pi}{6}\right)^{1/3} k_B n^{2/3} \sum v_i \left(\frac{T}{\Theta_i}\right)^2 \int_0^{\frac{\Theta_i}{T}} \frac{x^3 e^x}{(e^x-1)^2} dx. \quad (1)$$

Here, i is the polarization index, v_i is the speed of sound, $\Theta_i = v_i(\hbar/k_B)(6\pi^2 n)^{1/3}$ is the Debye temperature (i.e., cutoff frequency for each of the polarization), k_B is the Boltzmann constant, $\hbar$ is the reduced Planck's constant, and $x = \Theta_i/T$. We determine the sound speeds from our measurements of Young's modulus (tabulated in Table I and plotted as a function of mass density in the inset of Fig. 2) with the procedure detailed in Ref. [7]. The Young's modulus increases with the increase in mass density as shown in the inset of the plot of Fig. 2.

As shown in Fig. 2, the measured thermal conductivity and the minimum thermal conductivity predictions match well for our a-SiC:H thin films for lower densities ($< 2.2\,\mathrm{g\,cm^{-3}}$). However, for higher densities, the minimum thermal conductivity model underpredicts our measurements, which indicates that the mechanism of heat transfer in these amorphous films is different than that assumed by the minimum thermal conductivity model. More specifically, the notion that energy is mainly transferred through diffusion of thermal energy predominantly between nonpropagating modes, as has been shown to be applicable for a range of amorphous solids [41], is not valid for a-SiC:H. It is also worth noting that the concentration of hydrogen atoms in our a-SiC:H films (for the range of concentrations as shown in Table I) does not influence thermal transport. Although the hydrogen content in $2.5\,\mathrm{g\,cm^{-3}}$ and $2.9\,\mathrm{g\,cm^{-3}}$ are similar, the measured thermal conductivities are vastly different. Similarly, we also cannot ascribe the variation of thermal conductivities for our films on the relative silicon and carbon concentrations. Taken together, the mechanism of heat transfer in thin films of a-SiC:H cannot solely be attributed to diffusive energy transfer between nonpropagating modes, nor to the specific concentrations of the constituent atoms.

To gain more insight into the effect of mass density on the heat transfer mechanisms, we investigate the vibrational characteristics of our samples using FTIR spectroscopy. As shown in Fig. 3, the FTIR results show that the Si-C absorption band centered at approximately $760\,\mathrm{cm^{-1}}$ increases with increasing density. The increase in the Si-C absorption band is indicative of higher fractions of tetrahedrally bonded carbon atoms resulting in higher atomic coordination [6]. Thus, our FTIR measurements reveal that with increase in mass density, the vibrations associated with Si-C bonds (at 23 THz or $760\,\mathrm{cm^{-1}}$) increase substantially, changing the vibrational properties as well as the average coordination number, which ultimately results in the increase in the overall thermal conductivities (see Table I).

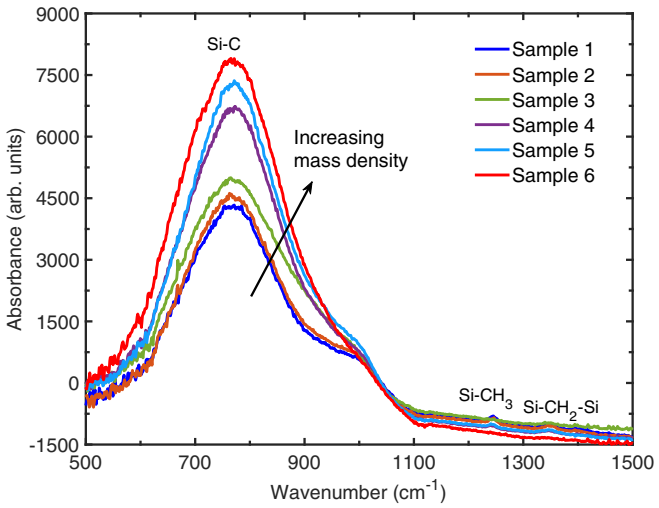

FIG. 3. Characteristic FTIR spectra (normalized to sample thickness) showing major absorption bands for amorphous SiC:H films. The Si-C absorption band increases with the increase of mass density of the a-SiC:H samples.

We note that Hondongwa *et al.* [7] measured the thermal conductivity of similar thin films of a-SiC:H. However, their reported values for films with relatively higher mass densities ($>2.3\,\mathrm{g\,cm^{-3}}$) are drastically higher than the values reported in this paper. This might be because of variations in the analysis procedures used in the two works. While Hondongwa *et al.* use the magnitude ($\sqrt{V_{in}^2 + V_{out}^2}$), we utilize the ratio (V_{in}/V_{out}) of the TDTR signal. For the determination of thermal conductivity in TDTR experiments, the use of magnitude can result in large uncertainties, whereas utilizing the ratio minimizes errors and allows us to measure thermal conductivity independent of laser power, variation in laser spot sizes as a function of delay time, changes in pump-probe spatial overlap, and the thermoreflectance coefficient of the metal transducer, which could all erroneously affect the predicted thermal conductivity if the magnitude is used instead [35,42].

III. MOLECULAR DYNAMICS SIMULATIONS AND LATTICE DYNAMICS CALCULATIONS

To gain atomistic insight into the role of density and microstructural coordination in amorphous silicon carbide systems, we perform MD simulations and LD calculations on a-SiC computational domains with varying mass densities. We study a-SiC instead of a-SiC:H in our atomistic simulations since the Tersoff interatomic potential has been well validated for the multicomponent silicon and carbon systems and has been shown to correctly predict various bulk physical properties for these materials [43–46]. However, to the best of our knowledge, similar optimized interatomic potentials for hydrogenated amorphous silicon carbide systems are still lacking in literature. Although the microstructural makeup of a-SiC:H might be different in comparison to a-SiC, our atomistic simulations are useful in understanding the different mechanisms that could potentially describe our experimental results on a-SiC:H systems. More specifically, our simulations

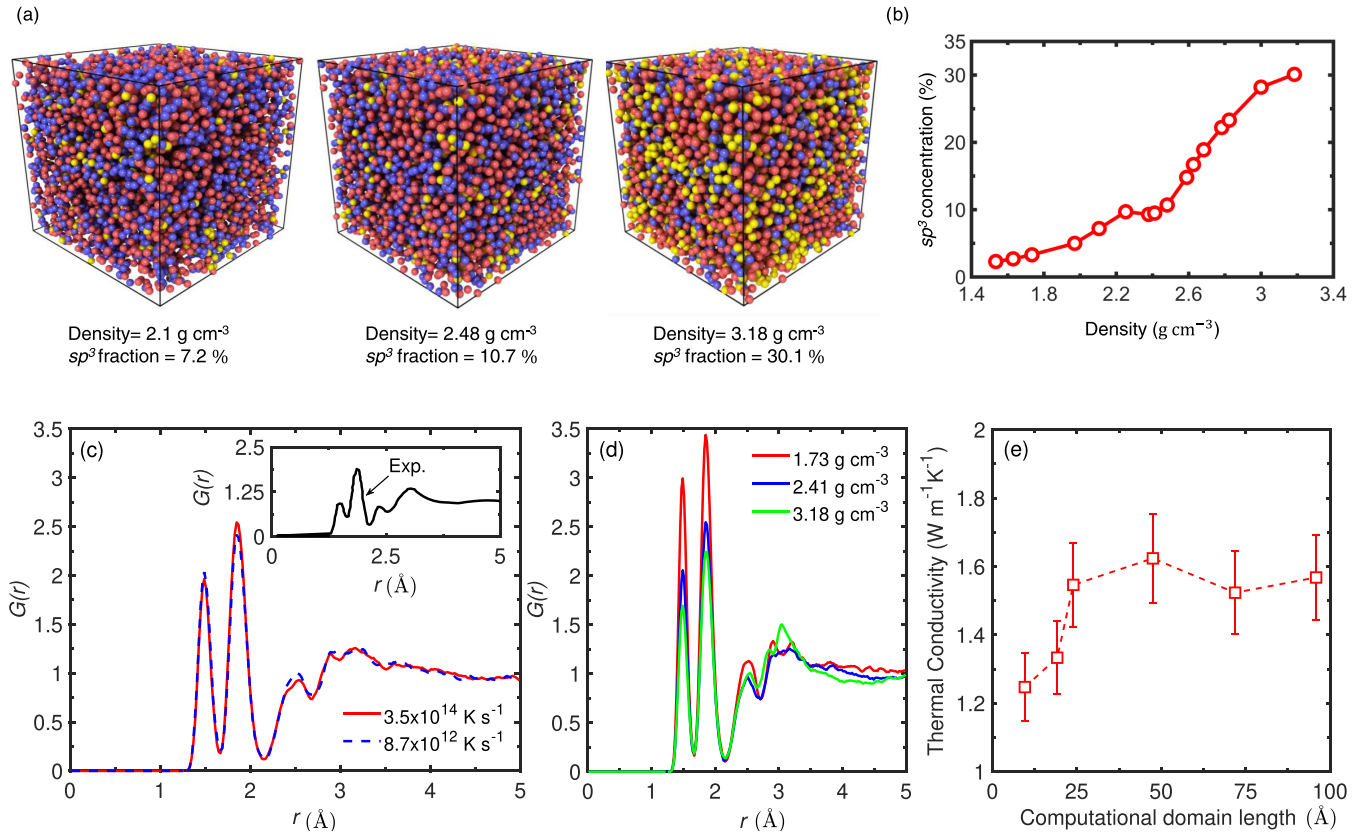

FIG. 4. (a) Computational domains of our amorphous silicon carbide (a-SiC) representing increasing ratios of sp^3 (yellow atoms) to sp^2 (blue atoms) bonded carbon atoms at three different densities; red atoms corresponds to silicon. (b) Concentration of sp^3-bonded carbon atoms as a function of the density showing a monotonic increase with the increase of density in the structure. (c) Radial distribution function at varying quench rates. For both quench rates, the C–C (∼1.5 nm), Si–C (∼1.86 nm), and Si–Si (∼2.52 nm) bond lengths agree very well with the experimental values as shown by the experimentally determined radial distribution function in the inset [49]. (d) Radial distribution function at varying mass densities, which shows that the C–C, Si–C, and Si–Si bond lengths are unaffected by varying the densities. (e) Thermal conductivity of our a-SiC structure with a mass density of 2.48 g cm^{-3} as a function of computational domain length. The thermal conductivity values converge for domain sizes larger than $\sim 25 \times 25 \times 25$ Å^3.

can provide insight into the role of carbon hybridization on heat transfer mechanism in a-SiC systems as we detail below.

Our MD simulations are conducted with the Large-scale Atomic/Molecular Massively Parallel Simulator (LAMMPS) [47] using the Tersoff potential [43]. Each simulation consists of 4000 carbon atoms and 4000 silicon atoms, for a total of 8000 atoms in our computational domains. To make our amorphous carbon domains, a crystalline SiC structure is initially melted at 9000 K, followed by rapidly quenching to 300 K at a quench rate of 8.7×10^{13} K s^{-1} to form an amorphous SiC structure. The structure is allowed to equilibrate under the Nośe-Hoover thermostat and barostat (with number of atoms, pressure and temperature held constant) for 1 ns at a prescribed temperature of 300 K. After equilibration, the volume of the simulation box is changed with atomic positions being remapped to mimic the amorphous structure at different densities. The computational domains are then annealed at 1100 K under the canonical ensemble with the number of atoms, volume, and temperature held constant for an additional 10 ns. This process removes any metastabilities as evidenced by the plateau in the potential energy during the annealing procedure [12,48]. Next, the structure is equilibrated under the canonical ensemble at room temperature for an additional 1 ns. Finally, the Green-Kubo (GK) formalism is used to determine the thermal conductivity of our equilibrated structures, which is given as

$$\kappa_\alpha = \frac{1}{k_B V T^2} \int_0^\infty \langle S_\alpha(t) S_\alpha(0) \rangle dt, \qquad (2)$$

where t is the time, T and V are the temperature and volume of the system, and $\langle S_\alpha(t) S_\alpha(0) \rangle$ is the αth component of the heat current autocorrelation function (HCACF). Here, the thermal conductivity is related to the integral of the HCACF, for which the values are collected for a total correlation time of 0.25 ps, and the simulation is run for another 5 ns.

Figure 4(a) shows our MD computational domains where the red atoms correspond to silicon, and yellow and blue atoms represent sp^3 and sp^2 hybridized carbons, respectively. To determine the sp^3 concentration of the SiC structures, atomic positions are extracted from our MD simulations and carbon atoms with fourfold coordination are identified. With increasing mass density, we find that the concentration of carbon atoms with a fourfold coordination increases

gradually. This is quantitatively shown in Fig. 4(b), showing the fraction of carbon atoms with sp^3 hybridization that increases monotonically as a function of mass density.

To gauge the local atomic structure of our computational model, we compute the radial distribution function given as [50]

$$G(r) = 4\pi[\rho(r) - \rho_0], \tag{3}$$

where $\rho(r)$ is the atomic density at a distance r from an atom in the computational domain and ρ_0 is the average atomic density. We compare $G(r)$ of our structures with the experimentally determined G(r) in Fig. 4(c) [49]. The calculated peaks at r positions of ∼1.5, 1.86, and 2.52 Å are assigned to C-C, Si-C, and Si-Si bonds, respectively [51,52]. Although the positions of the peaks match with the experimentally determined values [as shown in the inset of Fig. 4(c)], our calculations of the relative peak intensities, $G(r)$, at two different quench rates (of $3.5 \times 10^{14}\,\mathrm{K\,s^{-1}}$ and $8.7 \times 10^{12}\,\mathrm{K\,s^{-1}}$) do not exactly match the experimentally determined $G(r)$. This might be due to the insufficiencies of the Tersoff potential to fully replicate the experimentally determined structure of a-SiC. Since we are more concerned about providing the atomistic insights into the qualitative trends in our results, the Tersoff model utilized is sufficient for our purposes as we detail below. However, we note that more rigorous potentials such as those based on machine-learning approaches might be able to better capture the experimentally determined peak intensities, which is beyond the scope of the current paper but deserves further work.

As shown in Fig. 4(c), the quench rate in our simulations has no significant effect on our a-SiC structures described by the Tersoff potential. Moreover, we also compute the radial distribution functions at varying mass densities of $1.73\,\mathrm{g\,cm^{-3}}$, $2.41\,\mathrm{g\,cm^{-3}}$, and $3.18\,\mathrm{g\,cm^{-3}}$, as shown in Fig. 4(d); the r positions of the peaks are consistent for the different mass densities. Although there are slight changes in the peak heights of the radial distribution function, the C–C, C–Si, and Si–Si bond lengths in our structures are unaffected due to varying mass densities. Further, to ensure our results are not influenced by the size of our computational domain, we carried out a series of MD simulations by varying the simulation domain size from 10 Å to 96 Å, as shown in Fig. 4(e). The convergence of thermal conductivity within uncertainties for computational domain sizes greater than $25 \times 25 \times 25\,\mathrm{Å}^3$ ensures that our choice of the domain size does not influence our GK predictions.

Following our MD simulations, we utilize the GENERAL UTILITY LATTICE PROGRAM (GULP) to perform our LD calculations on the computational domains of amorphous silicon carbide obtained from our MD simulations. To estimate the contribution of diffusive, nonpropagating modes to thermal conductivity, we calculate the mode diffusivity based on the Allen and Feldman (A-F) theory [26] given as

$$\kappa_{\text{A-F}} = \sum_{\text{diffusons}} \frac{k_B}{V} D_{\text{A-F},j}(\omega_j), \tag{4}$$

where $D_{\text{A-F},j}$ is the harmonic mode diffusivity calculated from harmonic LD theory [26,48] and ω_j is the jth diffusion frequency. Propagon contribution to thermal conductivity, κ_{prop} can be approximated from

$$\kappa_{\text{total}} = \kappa_{\text{A-F}} + \kappa_{\text{propagon}}, \tag{5}$$

where κ_{total} is assumed to be equal to GK estimated thermal conductivity, since MD simulations intrinsically incorporate all types of vibrational modes in the spectrum (including propagating and nonpropagating modes).

To elucidate the role of atomic coordination on the vibrational characteristics, we calculate the vibrational density of states (DOS) for our structures with the varying mass densities and sp^3 concentrations. Figure 5(a) shows the DOS for three representative mass densities, where we observe that as mass density (and the concentration of sp^3 hybridized carbon atoms) increases, the DOS in the low-frequency range (< 10 THz) shifts to higher frequencies. Furthermore, we also observe an increase in the DOS of the higher frequency spectrum (> 15 THz). The relation between DOS and the vibrational frequencies for the lower frequency spectrum obeys the $\text{DOS}(\omega) \propto \omega^2$ relation, which is mostly applicable to long-wavelength propagating vibrations with group velocities corresponding to the speed of sound (under the Debye approximation). As mass density increases, the frequencies with the ω^2 relation [represented by the straight lines in Fig. 5(b)] also shift to higher frequencies, suggesting that the range of propagating modes in a-SiC increases with increasing fraction of sp^3 bonded carbon atoms. To further investigate the effect of carbon hybridization on the relative roles of propagating and nonpropagating modes, we calculate the diffusivities of the vibrational modes based on the A-F theory [26,27]. Figure 5(c) shows our calculated diffusivities for three computational domains with varying mass densities. The sharp decrease at high frequencies is characteristic of locons demonstrating their localized nature. As such, they contribute negligibly for all structures. For the low-frequency modes, the diffusivities are relatively higher, which is consistent with their propagating nature. Moreover, the onset of the Debye scaling as denoted by the cutoff frequencies in Fig. 5(c) is also consistent with our MD calculated DOS; note these modes are not included in the calculation of the thermal conductivity calculated by the A-F theory ($\kappa_{\text{A-F}}$). The diffusons with the relatively constant diffusivities (at the intermediate frequency spectrum) are responsible for ($\kappa_{\text{A-F}}$), where higher degrees of spatial overlap between the eigenvectors and the energetic overlap between the modes dictate their diffusivities. Therefore, the diffusivities of the modes for the lowest density case in Fig. 5(c) are comparatively lower than the higher density cases.

In Fig. 5(d), we compare the thermal conductivity predicted by the A-F theory with the results from our MD simulations under the GK formalism for our a-SiC computational domains at varying densities. Overall, both methods show a monotonic increase in thermal conductivity with increasing density. However, we observe a relatively higher increase for the GK-predicted thermal conductivities for structures with higher densities ($> 2.2\,\mathrm{g\,cm^{-3}}$). This suggests that the propagons (that are intrinsically included in our GK calculations while being neglected in the A-F theory) have a greater contribution at higher mass densities. We show this quantitatively in Fig. 5(e), where we plot the propagon contribution to the total thermal conductivity as a function of mass density. For lower densities ($< 2.2\,\mathrm{g\,cm^{-3}}$), the contribution increases

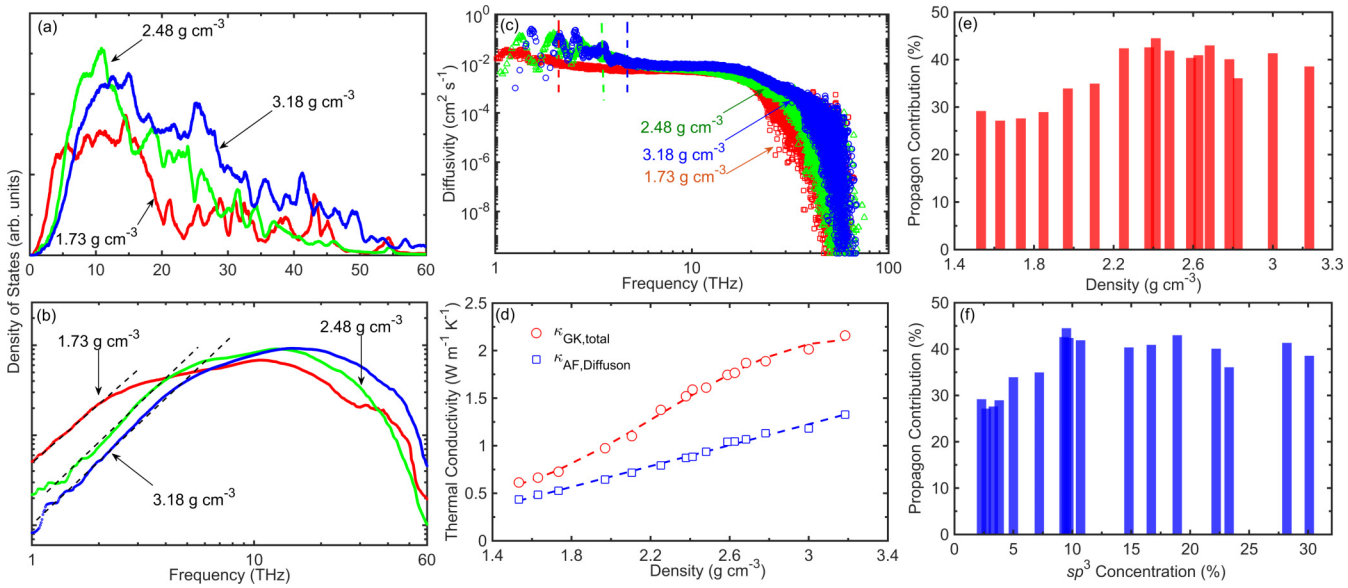

FIG. 5. (a) Vibrational density of states for low (1.78 g cm^{-3}), medium (2.48 g cm^{-3}), and high (3.18 g cm^{-3}) mass densities of amorphous silicon carbide. (b) Density of states showing its clear relationship to the ω^2 scaling at low frequencies. As shown by the dashed line, the Debye relation is most applicable to low frequency and long wavelength propagating modes. With the increase in the mass density of the structures, the cutoff frequency up to which the Debye relation is satisfied shifts to higher frequencies. (c) Mode diffusivities calculated for three different mass densities of our a-SiC computational domains based on the A-F theory. The cutoff frequencies for propagons are represented by the dashed lines. (d) Thermal conductivity as a function of mass density for a-SiC domains calculated based on the GK approach (circles) and the A-F theory for diffuson-driven thermal conductivity. Contributions from propagons to the total thermal conductivity in amorphous silicon carbide domain as a function of (e) mass density and (f) concentration of sp^3-bonded carbon atoms. The propagon contribution increases monotonically from ∼25% to ∼40% at low mass densities (< 2.2 g cm^{-3}) and sp^3 concentrations of carbon atoms (<10%), after which increasing the mass density or the fraction of sp^3-bonded carbon atoms does not result in higher contributions from propagons.

steadily from 25% to 40% and remains relatively constant for higher densities. This is also shown as a function of sp^3-bonded carbon fraction in the structures where for structures with greater than ∼8% sp^3 hybridized carbon concentration, we find that the propagon contributions are similar. Taken together, while the diffuson contribution increases monotonically for the entire mass density range studied in this paper, the propagon contribution steadily increases up to mass densities of 2.2 g cm^{-3} (or ∼10% sp^3 hybridized carbon concentration) and has a more significant contribution (of ∼40%) to the total thermal conductivity of a-SiC structures at mass densities > 2.2 g cm^{-3}. Therefore, these results point to the fact that through proper control of the local atomic coordination, we can tune the overall heat conduction and the intrinsic mechanisms responsible in dictating the thermal conductivity of a-SiC structures.

Finally, we compare our results from the MD simulations on our a-SiC structures to our experimental measurements of thermal conductivity for the a-SiC:H in Fig. 6. The increasing trend in thermal conductivity with mass density that we observe in our experiments is captured well with our GK predictions for the a-SiC structure. Even though in our experiments the concentration of hydrogen varies from 19% to 37% (see Table I), while our computational domains do not contain hydrogen atoms, the agreement in the TDTR-measured and MD-predicted thermal conductivities suggests that the heat transfer mechanism in the amorphous structures are similar. Moreover, the agreement also suggests that the concentration of hydrogen atoms in our a-SiC:H thin films (for the range of concentrations as shown in Table I) has negligible influence in dictating thermal transport in these amorphous silicon carbide-based systems. Taken together, our MD simulations and TDTR experiments comprehensively show that the thermal conductivity in these materials is mainly driven by changes in the mass density and atomic coordination.

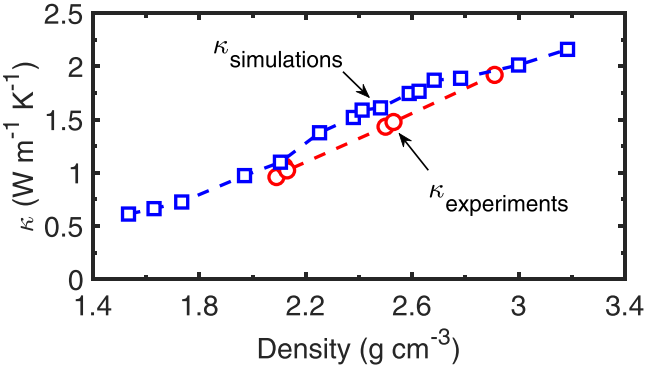

FIG. 6. Comparison between our experimentally measured thermal conductivities for our a-SiC:H samples and the Green-Kubo predicted thermal conductivities for our a-SiC domains. The agreement in the increasing trend in thermal conductivity between our experimental and computational results suggests that the heat transfer mechanisms are similar for the different structures with increasing mass densities.

IV. CONCLUSION

To summarize, we have studied the role of mass density and atomic coordination on the vibrational heat transfer mechanisms in amorphous silicon carbide systems through a combination of experiments and simulations. In particular, through chemical, mechanical, vibrational, and structural analysis in conjunction with TDTR measurements, our results show the significant role played by the coordination number and the mass density on the thermal conductivity of a-SiC:H. We show that the thermal conductivity increases monotonically (from $0.9\,\mathrm{W\,m^{-1}\,K^{-1}}$ to $1.9\,\mathrm{W\,m^{-1}\,K^{-1}}$) as mass density is increased from $2\,\mathrm{g\,cm^{-3}}$ to $2.9\,\mathrm{g\,cm^{-3}}$. Our FTIR results point to the fact that the average atomic coordination is increased with increasing mass density for these films, thus revealing a possible mechanism that can be utilized to manipulate the thermal conductivity in these materials. Our MD simulations in addition with LD calculations on a-SiC support our experimental findings and shed light on the implications of atomic coordination (and sp^3 content) on the contribution from the categorical vibrations in amorphous solids (i.e., diffusons and propagons) on the overall heat conduction in these structures. More specifically, our MD simulations show that the thermal conductivity of a-SiC increases by a factor of 4 with the increase in sp^3 hybridized carbon atoms from ∼3% to ∼30%. The contribution from propagating modes to the overall thermal conductivity in a-SiC can be increased from ∼25% to ∼40% by increasing the fraction of sp^3 bonded carbon atoms to $\geqslant 10\%$ (or above densities of $\sim 2.2\,\mathrm{g\,cm^{-3}}$). On the contrary, the contribution from the nonpropagating modes (or diffusons) increases monotonically throughout the density range (from 1.5 to $3.2\,\mathrm{g\,cm^{-3}}$). Our results elucidate the fundamental role of microstructure in determining the heat transfer mechanisms in amorphous silicon carbide systems, thus opening a route to tuning their physical properties based on manipulating the carbon hydridization.

ACKNOWLEDGMENTS

This work is supported by the Office of Naval Research, Grants No. N00014-21-1-2622 and No. N00014-20-1-2686, and the Semiconductor Research Corporation, Grant No. 2021-NM-3047.

[1] A. Grill, S. M. Gates, T. E. Ryan, S. V. Nguyen, and D. Priyadarshini, Appl. Phys. Rev. **1**, 011306 (2014).
[2] M. Köhler, M. Pomaska, P. Procel, R. Santbergen, A. Zamchiy, B. Macco, A. Lambertz, W. Duan, P. Cao, B. Klingebiel *et al.*, Nat. Energy **6**, 529 (2021).
[3] Y. Hamakawa, *Amorphous and Crystalline Silicon Carbide II*, edited by M. M. Rahman, C. Y.-W. Yang, and G. L. Harris (Springer, Berlin, Heidelberg, 1989), pp. 164–170.
[4] D.-S. Wuu, R.-H. Horng, C.-C. Chan, and Y.-S. Lee, Appl. Surf. Sci. **144**, 708 (1999).
[5] I. Spitsberg and J. Steibel, Int. J. Appl. Ceram. Technol. **1**, 291 (2004).
[6] S. W. King, J. Bielefeld, G. Xu, W. A. Lanford, Y. Matsuda, R. H. Dauskardt, N. Kim, D. Hondongwa, L. Olasov, B. Daly *et al.*, J. Non-Cryst. Solids **379**, 67 (2013).
[7] D. Hondongwa, L. Olasov, B. Daly, S. King, and J. Bielefeld, Thin Solid Films **519**, 7895 (2011).
[8] A. Giri, C. J. Dionne, and P. E. Hopkins, npj Comput. Mater. **8**, 55 (2022).
[9] J. L. Braun, S. W. King, E. R. Hoglund, M. A. Gharacheh, E. A. Scott, A. Giri, J. A. Tomko, J. T. Gaskins, A. Al-Kukhun, G. Bhattarai, M. M. Paquette, G. Chollon, B. Willey, G. A. Antonelli, D. W. Gidley, J. Hwang, J. M. Howe, and P. E. Hopkins, Phys. Rev. Materials **5**, 035604 (2021).
[10] A. Einstein, Ann. Phys. **340**, 898 (1911).
[11] J. L. Braun, C. H. Baker, A. Giri, M. Elahi, K. Artyushkova, T. E. Beechem, P. M. Norris, Z. C. Leseman, J. T. Gaskins, and P. E. Hopkins, Phys. Rev. B **93**, 140201(R) (2016).
[12] J. M. Larkin and A. J. H. McGaughey, Phys. Rev. B **89**, 144303 (2014).
[13] S. Kwon, J. Zheng, M. C. Wingert, S. Cui, and R. Chen, ACS Nano **11**, 2470 (2017).
[14] K. T. Regner, D. P. Sellan, Z. Su, C. H. Amon, A. J. H. McGaughey, and J. A. Malen, Nat. Commun. **4**, 1640 (2013).
[15] R. Costescu, D. Cahill, F. Fabreguette, Z. Sechrist, and S. George, Science **303**, 989 (2004).
[16] G. Pernot, M. Stoffel, I. Savic, F. Pezzoli, P. Chen, G. Savelli, A. Jacquot, J. Schumann, U. Denker, I. Mönch *et al.*, Nat. Mater. **9**, 491 (2010).
[17] C. Chiritescu, D. G. Cahill, N. Nguyen, D. Johnson, A. Bodapati, P. Keblinski, and P. Zschack, Science **315**, 351 (2007).
[18] M. D. Losego, I. P. Blitz, R. A. Vaia, D. G. Cahill, and P. V. Braun, Nano Lett. **13**, 2215 (2013).
[19] P. E. Hopkins, M. Mittal, L. M. Phinney, A. M. Grillet, and E. M. Furst, Appl. Phys. Lett. **99**, 133106 (2011).
[20] A. Giri, J.-P. Niemelä, T. Tynell, J. T. Gaskins, B. F. Donovan, M. Karppinen, and P. E. Hopkins, Phys. Rev. B **93**, 115310 (2016).
[21] Y. S. Ju, M.-T. Hung, M. Carey, M.-C. Cyrille, and J. Childress, Appl. Phys. Lett. **86**, 203113 (2005).
[22] J. C. Duda, P. E. Hopkins, Y. Shen, and M. C. Gupta, Appl. Phys. Lett. **102**, 251912 (2013).
[23] J. C. Duda, P. E. Hopkins, Y. Shen, and M. C. Gupta, Phys. Rev. Lett. **110**, 015902 (2013).
[24] X. Wang, C. D. Liman, N. D. Treat, M. L. Chabinyc, and D. G. Cahill, Phys. Rev. B **88**, 075310 (2013).
[25] J. Olson, K. Topp, and R. Pohl, Science **259**, 1145 (1993).
[26] P. B. Allen and J. L. Feldman, Phys. Rev. B **48**, 12581 (1993).
[27] P. B. Allen, J. L. Feldman, J. Fabian, and F. Wooten, Philos. Mag. B **79**, 1715 (1999).
[28] M. Zebarjadi, K. Esfarjani, M. Dresselhaus, Z. Ren, and G. Chen, Energy Environ. Sci. **5**, 5147 (2012).
[29] N. P. Padture, M. Gell, and E. H. Jordan, Science **296**, 280 (2002).
[30] A. Giri, S. W. King, W. A. Lanford, A. B. Mei, D. Merrill, L. Li, R. Oviedo, J. Richards, D. H. Olson, J. L. Braun *et al.*, Adv. Mater. **30**, 1804097 (2018).

[31] T. Pomorski, B. Bittel, C. Cochrane, P. Lenahan, J. Bielefeld, and S. King, J. Appl. Phys. **114**, 074501 (2013).
[32] S. King, M. French, J. Bielefeld, and W. Lanford, J. Non-Cryst. Solids **357**, 2970 (2011).
[33] W. Lanford, M. Parenti, B. Nordell, M. Paquette, A. Caruso, M. Mäntymäki, J. Hämäläinen, M. Ritala, K. Klepper, V. Miikkulainen *et al.*, Nucl. Instrum. Methods Phys. Res., Sect. B **371**, 211 (2016).
[34] A. J. Schmidt, Optical characterization of thermal transport from the nanoscale to the macroscale, Ph.D. thesis, Massachusetts Institute of Technology, 2008.
[35] D. G. Cahill, Rev. Sci. Instrum. **75**, 5119 (2004).
[36] P. E. Hopkins, J. R. Serrano, L. M. Phinney, S. P. Kearney, T. W. Grasser, and C. T. Harris, J. Heat Transfer **132**, 081302 (2010).
[37] G. Tas and H. J. Maris, Phys. Rev. B **49**, 15046 (1994).
[38] C. Thomsen, J. Strait, Z. Vardeny, H. J. Maris, J. Tauc, and J. J. Hauser, Phys. Rev. Lett. **53**, 989 (1984).
[39] C. Y. Ho, R. W. Powell, and P. E. Liley, J. Phys. Chem. Ref. Data **1**, 279 (1972).
[40] D. G. Cahill, S. K. Watson, and R. O. Pohl, Phys. Rev. B **46**, 6131 (1992).
[41] M. T. Agne, R. Hanus, and G. J. Snyder, Energy Environ. Sci. **11**, 609 (2018).
[42] R. M. Costescu, M. A. Wall, and D. G. Cahill, Phys. Rev. B **67**, 054302 (2003).
[43] J. Tersoff, Phys. Rev. B **39**, 5566 (1989).
[44] J. Tersoff, Phys. Rev. B **49**, 16349 (1994).
[45] K. Xue, L.-S. Niu, and H.-J. Shi, J. Appl. Phys. **104**, 053518 (2008).
[46] V. I. Ivashchenko, P. E. A. Turchi, and V. I. Shevchenko, Phys. Rev. B **75**, 085209 (2007).
[47] S. Plimpton, J. Comput. Phys. **117**, 1 (1995).
[48] J. L. Feldman, P. B. Allen, and S. R. Bickham, Phys. Rev. B **59**, 3551 (1999).
[49] M. Ishimaru, I.-T. Bae, Y. Hirotsu, S. Matsumura, and K. E. Sickafus, Phys. Rev. Lett. **89**, 055502 (2002).
[50] Z. Sha, P. Branicio, Q. Pei, V. Sorkin, and Y. Zhang, Comput. Mater. Sci. **67**, 146 (2013).
[51] F. Finocchi, G. Galli, M. Parrinello, and C. M. Bertoni, Phys. Rev. Lett. **68**, 3044 (1992).
[52] D. Mura, L. Colombo, R. Bertoncini, and G. Mula, Phys. Rev. B **58**, 10357 (1998).